Progress In Electromagnetics Research, Vol. 128, 75–90, 2012

STUDY OF MAGNETIC GRAVITY COMPENSATOR TOPOLOGIES USING AN ABSTRACTION IN THE ANALYTICAL INTERACTION EQUATIONS

J. L. G. Janssen*, J. J. H. Paulides, and E. A. Lomonova

Eindhoven University of Technology, Electrical Engineering, Electromechanics and Power Electronics, P. O. Box 513, 5600MB Eindhoven, The Netherlands

Abstract—This paper identifies an abstraction that is found in the equations that describe the 3D interaction between cuboidal permanent magnets and applies this to the magnetic design of a gravity compensator. It shows how the force between magnets and its position-sensitivity, important design parameters for magnetically levitated 6-DoF gravity compensators, may be translated into the magnetic domain and verifies this with 3D analytical models. With this information, a number of basic gravity compensator topologies is derived. These topologies are subsequently investigated in more detail, with specific focus on combining a high force with low position sensitivity.

1. INTRODUCTION

Many techniques and technologies have been developed over time to suppress disturbances in vibration-sensitive equipment [1]. One of the components in these anti-vibration devices provides the vertical force that is necessary to compensate the isolated object's gravity force. As opposed from the more established technologies such as hydraulic, mechanical or pneumatic systems, fully electromagnetic gravity compensators represent a relatively new technology in vibration isolation. Despite their reduced force density, technological immaturity and design complexity they offer the advantages of a low stiffness, a high isolation bandwidth and low static energy consumption [2–4].

The properties of vibration isolation systems are often expressed in terms of force, damping and resonance frequency [1–3]. Many

Received 14 October 2011, Accepted 7 May 2012, Scheduled 18 May 2012

* Corresponding author: Jeroen Lodevicus Gerardus Janssen (j.l.g.janssen@tue.nl).

of these devices exhibit a high vertical force, to compensate the gravitational force of the isolated platform, with very low stiffness, which results in insensitivity to floor vibrations. In the design of the aforementioned electromagnetic devices it is considered helpful to describe these (mechanical) properties in the electromagnetic domain. Such transcription is performed in this paper using the analytical surface charge modeling technique, as is described in Section 2. Section 3 applies the general findings to a topology with two magnets and in Sections 4 and 5 they are applied to multi-magnet structures, followed by the conclusions in Section 6.

2. ABSTRACTION OF THE ANALYTICAL MODEL

The analytical surface charge model is an elegant way to evaluate electromechanical properties of magnet structures [2, 3, 5–8]. It provides an elegant, fully 3D and mesh-free computation of the field, which is extremely accurate and time inexpensive, especially compared to numerical methods such as finite element analysis (FEA). It is based on a scalar potential formulation of Maxwell's equations. The most important assumption of this static model assumes are that the relative permeability of the permanent magnets $\mu_r = 1$, which has a small but well-predictable influence on the force as is experimentally shown in [3, 5, 7, 8]. Further, the magnetization within the magnets is uniform. If the magnetization vector $\vec{M}$ [A/m] is confined to the magnet volume V [m^3] with surface S [m^2], constant within this volume and falls abruptly to zero outside it, a scalar potential Ψ [A] is derived from the field $\vec{H}$ [A/m] by [5, 9]

$$-\nabla\Psi = \vec{H}, \quad \Psi = \int_S \frac{\sigma_m(\vec{x}\,')}{|\vec{x} - \vec{x}\,'|} ds', \quad \sigma_m = \vec{M} \cdot \vec{\hat{n}}, \tag{1}$$

where σ_m [A/m] is the magnetic surface charge density and the primed variables $\vec{x}\,'$ and s' are intermediate integration variables that result from the solution of Green's function. $\vec{\hat{n}}$ is the unitless outward normal vector of volume V.

The resulting equation for the magnetic flux density $\vec{B}(\vec{x})$ [T] is given by [5, 9]

$$\vec{B}(\vec{x}) = \frac{\vec{B_r}}{4\pi} \int_S \frac{\sigma_m(\vec{x}\,')(\vec{x} - \vec{x}\,')}{|\vec{x} - \vec{x}\,'|^3} d\vec{s}'. \tag{2}$$

The remanent magnetization is given by $B_r = \mu_0 M$ [T], with $\mu_0 = 4\pi 10^{-7}$ [H/m] being the magnetic permeability of vacuum. This notation represents the permanent magnet as an equivalent

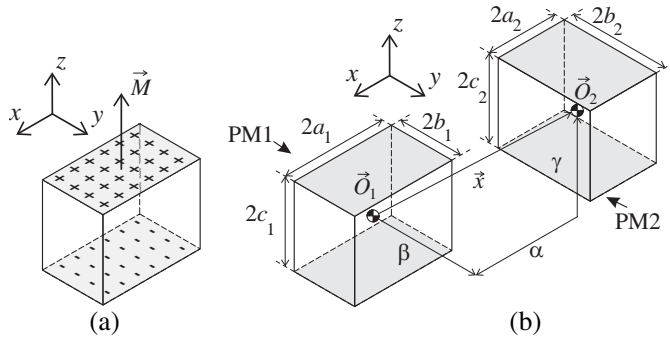

Figure 1. Impression of (a) the magnetic surface charge of a magnet and (b) the dimensions of two permanent magnets PM1 and PM2. Their interaction force may be obtained by integrating PM1's field over the grey surfaces of PM2.

distribution of magnetic surface charge σ_m. As Fig. 1(a) shows, this surface charge is located on the surfaces perpendicular to the magnetization vector of the magnet PM1 which has the dimensions $[2a_1, 2b_1, 2c_1]$. The resulting field equations for permanent magnet 1 (PM1) in Fig. 1(b) are then given by [5, 9]

$$\vec{B}(\vec{x}) = \frac{B_r}{4\pi} \sum_{i=0}^{1} \sum_{k=0}^{1} \sum_{p=0}^{1} (-1)^{i+k+p} \begin{pmatrix} \log(R-T) \\ \log(R-S) \\ \operatorname{atan}\left(\dfrac{ST}{RU}\right) \end{pmatrix}, \tag{3}$$

$$S = x - (-1)^i a_1, \quad T = y - (-1)^k b_1, \tag{4}$$

$$U = z - (-1)^p c_1, \quad R = \sqrt{S^2 + T^2 + U^2}. \tag{5}$$

If the superposition principle is employed, it is possible to model the field of multiple magnets and to model cuboidal magnets with an arbitrary magnetization vector [3, 7, 8, 10].

Equations (1), (2) and Fig. 1(a) show that the permanent magnet is represented by two surfaces with a magnetic surface charge. These equivalent magnetic surface charges are a mathematical manner to derive the necessary energy, field or interaction equations [11].

2.1. Force Calculation

The dimensions of the second magnet PM2 are $[2a_2, 2b_2, 2c_2]$ and its displacement is given by $[\alpha, \beta, \gamma]$. The analytical equations that describe the interaction force between these permanent magnets, based

on the surface charge model, have been successfully derived and validated with experiments and FEA in [3, 5–8]. The force between two permanent magnets may be obtained with Virtual work [5, 8] or by the Lorentz force method [3, 6, 7]. The latter becomes

$$\vec{F}\left(\vec{x}\,'\right) = \int_{S_2} \sigma_m\left(\vec{x}\,'\right) \vec{B}_1\left(\vec{x}\,'\right) ds'. \tag{6}$$

This methods consists of a surface integral of the first magnet's flux density $\vec{B}_1$ over the second magnet's surface S_2. The equations then obtain the general form

$$\vec{F}(\vec{x}\,) = \frac{B_{r_1} B_{r_2}}{4\pi\mu_0} \sum_{\substack{i,j,k=0 \\ l,m,n=0}}^{1} (-1)^{i+j+k+l+m+n} \vec{\xi}(u,v,w), \tag{7}$$

$$u = \alpha - (-1)^i a_1 + (-1)^j a_2, \quad v = \beta - (-1)^k b_1 + (-1)^l b_2, \tag{8}$$

$$w = \gamma - (-1)^m c_1 + (-1)^n c_2, \quad r = \sqrt{u^2 + v^2 + w^2}. \tag{9}$$

The variable $\vec{\xi}$ is a vector of equations which depends on the dimensions of both magnets and their relative displacement, as shown in Fig. 1(b). The analytical form of this vector has been derived and validated in [5, 6] (parallel magnetization) and in [3, 7, 8] (perpendicular magnetization).

As (6) shows, the integrand in the Lorentz force equation (6) concerns a multiplication of the flux density $\vec{B}_1$ over the second magnet's surfaces which have a magnetic charge density σ_m. If this second magnet is magnetized vertically these are the top and bottom surfaces of PM2 according (1). After integration the magnitude of the force $\vec{F}$ is defined by σ_{m_2}, $\vec{B}_1$ and the integration limits of (6), which are the dimensions of PM2. This suggest that an evaluation of PM1's field $\vec{B}_1$ and the magnetization direction and dimensions of PM2 are sufficient to predict the force between two permanent magnets as is summarized in Table 1. A calculation of PM2's field is not necessary. Naturally, a high value of $\vec{B}_1$ on the side surfaces of PM2, which is obtained when the distance between them is small, results in a high force. However, it is the combination with stiffness requirements that render this new abstraction useful for the design of gravity compensators.

2.2. Stiffness Calculation

The 3-by-3 stiffness matrix $\mathbf{K}$ is defined by

$$\mathbf{K} = -J\vec{F}. \tag{10}$$

Table 1. The interaction force and stiffness can be estimated from PM1's flux density's magnitude and gradient at the location of PM2.

Mech. domain	Electromagnetic domain
Force	Flux density of integrated over magnet surface
Stiffness	Gradient of flux density near the magnet edges

J is the Jacobian, or matrix of all first-order partial derivatives of the force vector. The resulting 3x3 stiffness matrix $\mathbf{K}$ is analytically derived and validated in [12] and not elaborated on here. However, with the knowledge that stiffness is the sensitivity of the force in (6) to displacements an abstraction similar to that for the force is derived. This force is the result of an integral over a magnet surface; as such, its sensitivity to displacements is given by the field gradients around its integration limits, or the edges of the surface. If PM2 is displaced, these limits shift accordingly. A field gradient around these limits causes a position-dependent change in the integral, hence, a force variation, causes increased stiffness. A reduction of stiffness is therefore accomplished by reducing the field gradients around the second magnet's edges as is summarized in Table 1. As a result, the magnetic flux that crosses the integration surface remains almost constant if the second magnet is displaced. However, a low field gradient generally contradicts with the high magnetic field that is required to obtain a high force, as is discussed below.

3. COMBINING A LARGE FORCE WITH LOW STIFFNESS

As mentioned, a gravity compensator in a anti-vibration device requires low displacement sensitivity of the vertical force [1–4]. This device's resonance frequency f_r [Hz] may be expressed in terms of vertical force F_z [N] and stiffness K_{zz} [N/m] by

$$f_r = 2\pi\sqrt{\frac{K_{zz}}{m}} = 2\pi\sqrt{\frac{gK_{zz}}{F_z}}\,, \tag{11}$$

where m [kg] is the mass, and $g = 9.81\,[\mathrm{m/s^2}]$ is the gravitational acceleration. For permanent-magnet based isolation systems it is challenging to obtain such low resonance frequency. The force in the basic topology of Fig. 2(a) [13] has an inverse exponential relation with the distance between the magnets and is therefore incapable of meeting these requirements. The topology shown in Fig. 2(b) overcomes this compromise by placing a positive and a negative magnetic spring

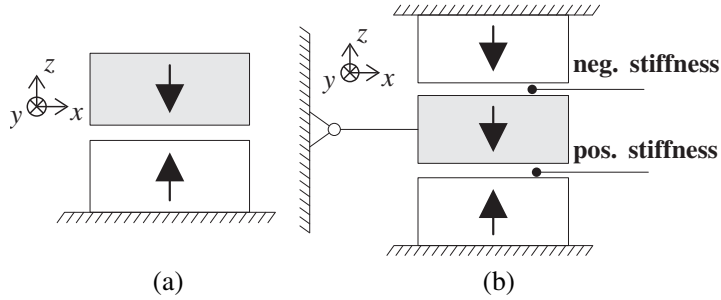

Figure 2. Magnet topology with (a) two repelling magnets and (b) a combination of repulsion and attraction in two parallel horizontal airgaps. The floating magnets are colored grey.

in parallel; the forces in both airgaps sum up, whilst their stiffness cancels [2, 4]. In terms of manufacturing complexity and tolerance sensitivity this is more difficult than a single-airgap topology. This paper aims at reducing stiffness with a single-airgap topology to reduce manufacturing complexity and to maintain a low vertical profile. Such basic topologies were proposed in [14, 15] and are studied in more detail in this paper.

3.1. Field Analysis

Figure 3 shows the 2D equipotential contours of a single vertically magnetized permanent magnet. The width of this magnet is 20 mm and its height is 10 mm. The potential formulation that is used is the 2D form of the scalar potential [9]. The magnitude of the magnetic flux density $\vec{B}$ is related to the density of these equipotential lines and the variation in intermediate distance is a measure for the gradient. density and their gradient are both large, which suggests high force capabilities but also high position dependency of this force.

As discussed in Section 2.1 it is sufficient to observe the field of this single permanent magnet to estimate its interaction force with another permanent magnet. The horizontal line in Fig. 3 may represent the bottom surface of this second permanent magnet, PM2. Figs 4(a) and (b) show the 2D magnetic flux density components on this line as function of the distance between this line and the magnet, which is varied between 0 mm and 6 mm. At small airgap values, the vertical flux density component in Fig. 4(a) is reasonably constant above the magnet and exhibits large gradients around the magnet edges. Therefore, a topology that simultaneously exhibits a large force and low

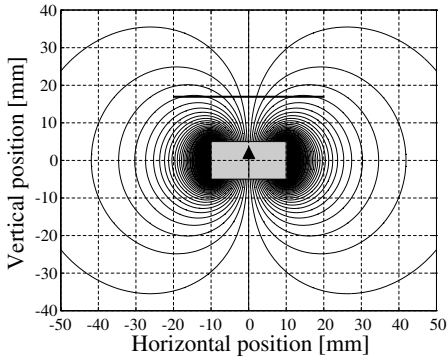

Figure 3. The equipotential contours of a single permanent magnet modeled with an analytical 2D surface charge model [9]. The magnet is colored grey and is magnetized along the vertical axis. The thick black line is used to evaluate the field results in Fig. 4.

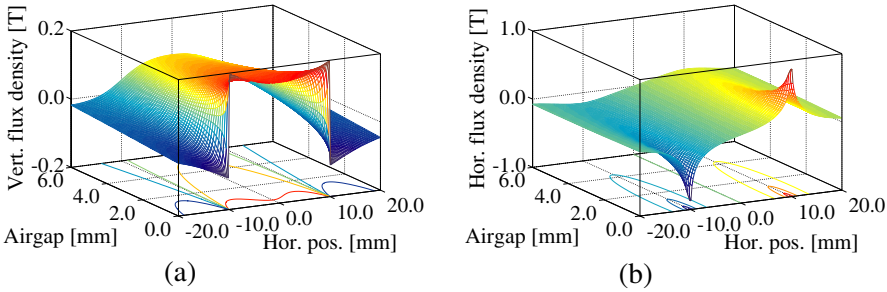

Figure 4. The (a) vertical and (b) horizontal flux density components above the magnet on the thick horizontal line in Fig. 3. The distance between this line and the magnets is indicated by 'airgap'.

stiffness should have the second magnet placed such, that its leading edges remain in the low-gradient parts of Fig. 4.

3.2. Basic Topology Identification

Figure 5(a) shows the 3D configuration of two permanent magnets with dimensions $40 \times 40 \times 10$ mm, a separation of 1.5 mm and a remanent flux density $B_r = 1.23$ T. This is an intuitive and well-known magnet configuration to obtain a large vertical force. Fig. 5(b) shows the three force components as function of the displacement along x. As well the horizontal component F_x as the vertical component F_z are strongly

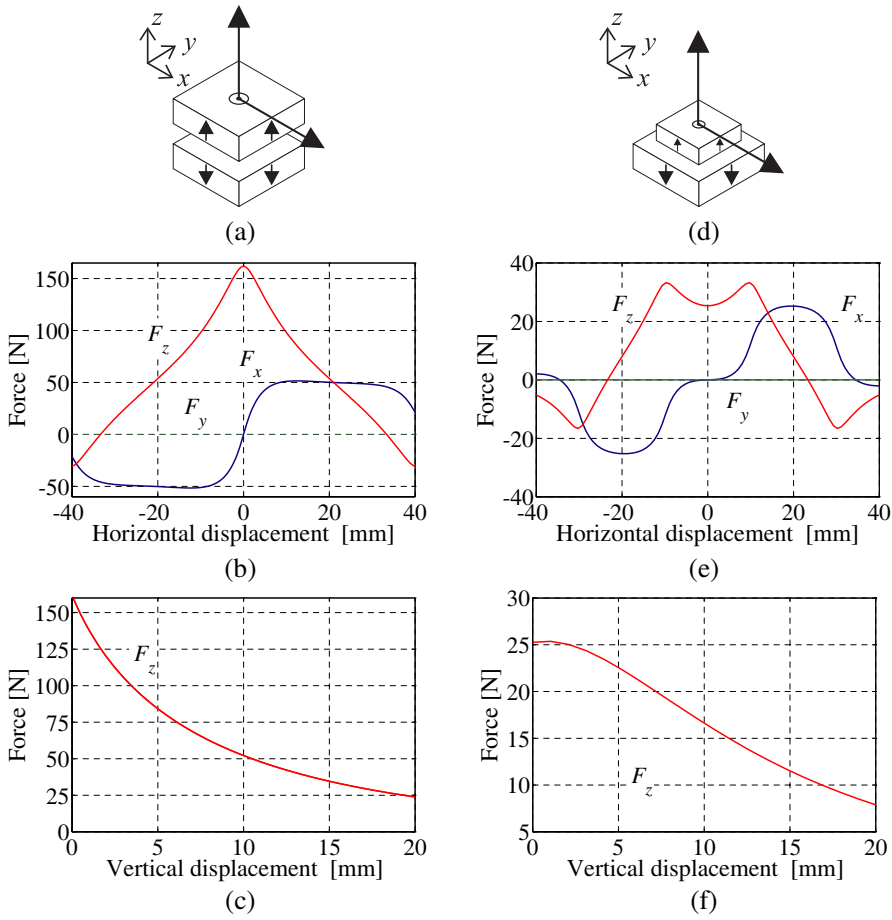

Figure 5. (a) The topology with equally sized magnets and the force components as function of of (b) horizontal and (c) vertical displacement along x and z, respectively. In (d) the top magnet's dimensions has reduced, which has en effect the force as function of (e) horizontal and (f) vertical displacement along x and z, respectively.

position dependent around zero. Fig. 5(c) shows the strong influence of vertical displacement on the force, especially for low displacement values. The gradient, or stiffness, decreases rapidly with z, however, the force reduces accordingly. As such, this topology is most probably unsuitable for the envisaged gravity compensator.

In the topology of Fig. 5(d) the top magnet's dimensions have reduced to $20 \times 20 \times 8\,\text{mm}$, which eliminates the sharp gradients of

Fig. 4 in the integral for the force [16]. Figs. 5(e) and 5(f) show that the vertical force has reduced with respect to the other topology. However, its stiffness is low and even becomes negative for zero vertical displacement (according (10)). Compared to the topology in Fig. 5(a), this stiffness is significantly lower and less dependent on displacements. As such, this topology shows more potential, although the effect of the observed force reduction needs to be investigated.

A third possible topology is obtained from the results in Fig. 5(b); if a horizontal offset displacement of 20 mm is chosen, the horizontal force F_x becomes virtually position independent. By rotating the topology 90° around its this y-axis (Fig. 6(a)) this F_x component becomes the vertical gravity compensating force component [3, 15]. The remaining F_z component of Fig. 5(b), along with its position dependency, is canceled by the stacked topology of Fig. 6(b). The lowest magnet on the left hand side is attracted by the right hand magnet and experiences a horizontal force along $+z$ and a vertical force along $-x$. Simultaneously, the upper magnet is repelled and experiences a force along $-z$ and $-x$. The result is an exactly vertical net force vector on the magnets at zero stiffness. As such, this topology is capable of producing a large vertical force, which is almost position independent.

4. OPTIMIZATION OF HORIZONTAL TOPOLOGIES

This section investigates the suitability of the basic topologies that exhibit a horizontal airgap. The volume of this gravity compensator is used as a constraint (a cube with sides of 250 mm) and it is investigated how the required force level F_z (between 1 kN and 10 kN) affects the minimization of the vertical stiffness K_{zz}. The permanent magnets exhibit a remanence $B_r = 1.23$ T and $\mu_r = 1$.

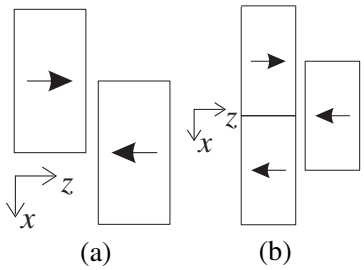

Figure 6. Rotation of the basic magnet topology (a) and (b) the elimination of the horizontal force component.

4.1. Arrays with Equal Dimensions

This section discusses the optimization of the topologies shown in Fig. 7, which are based on Fig. 5(a). The dimensions shown in Fig. 8 correspond to the topology in Fig. 7(c), which has a quasi-Halbach magnetization pattern. The number of magnetic pole pitches τ_p along the horizontal directions defines the variable n, hence, equals $n = 3$ in this case. The width of the array is given by $n\tau_p$. If the magnet pitch τ_m is chosen equal to the pole pitch τ_p this results in the topology shown in Fig. 7(b). If $n = 1$, this results in the topology of Fig. 7(a).

The optimization is performed with a nonlinear unconstrained multi-variable optimization (Matlab's fmincon). It is defined by the function

$$\vec{x}^* = \min_{\vec{x}\in\vec{X}} \left\{ \mathcal{G}_K(\vec{x}) \mid \vec{c}(\vec{x}) \leq 0,\ \ \vec{c}_{\text{eq}}(\vec{x}) = 0, \vec{X} \subset \mathbb{R}^n \right\}. \tag{12}$$

$\mathcal{G}(\vec{x})$ is the objective function of the vector of variables $\vec{x}$ and is minimized. The nonlinear inequality constraints are described by

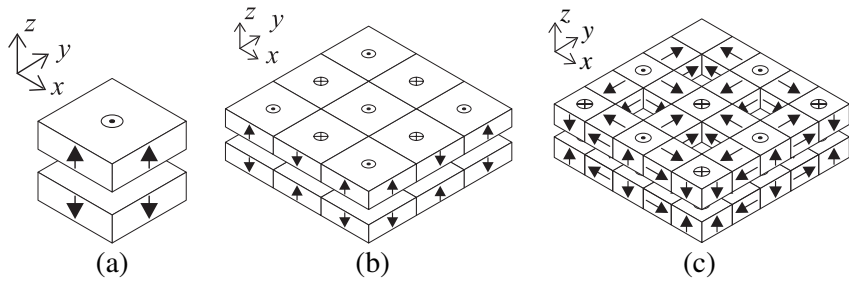

Figure 7. Gravity compensator topologies with (a) $n = 1$, (b) $\tau_m = \tau_p$ and (c) a quasi-halbach topology.

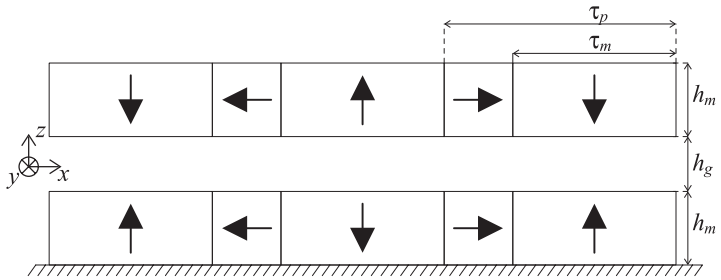

Figure 8. Dimensions of the gravity compensator with equally sized magnet arrays. This example has three poles in each horizontal direction, hence $n = 3$.

$\vec{c}(\vec{x})$ and the nonlinear equality constraints by $\vec{c}_{\mathrm{eq}}(\vec{x})$. The objective function is formulated by

$$\mathcal{G}_K(\vec{x}) = \left(K_{zz} - 1.00\,\mathrm{kN/m}\right)^2. \tag{13}$$

It aims to bring the vertical stiffness as close to 1.00 kN/m as possible. A minimization towards minus infinity has not been performed to prevent negative vertical stiffness values. The vector of variables $\vec{x}$ is subject to linear constraints on the variables in Fig. 8.

$$\vec{x} = \begin{bmatrix} n\tau_p/250\,\mathrm{mm} \\ \tau_m/\tau_p \\ h_m/\tau_p \\ h_g/15\,\mathrm{mm} \end{bmatrix}, \quad \begin{bmatrix} 0.5 \\ 0.3 \\ 0.25 \\ 0.1 \end{bmatrix} \leq \vec{x} \leq \begin{bmatrix} 1.5 \\ 1 \\ 4 \\ 10 \end{bmatrix}. \tag{14}$$

The first term $n\tau_p/250\,\mathrm{mm}$ limits the width of the array and the second term τ_m/τ_p the pitch ratio. The third term h_m/τ_p constraints the height of the magnets and the fourth term $h_g/15\,\mathrm{mm}$ limits the airgap length to its minimum value of 1.5 mm.

The nonlinear equality constraint $\vec{c}_{\mathrm{eq}}(\vec{x})$ applies to the vertical force $F_z(\vec{x})$ which must equal a target force F_t which is varied between 1 kN and 10 kN in steps of 500 N.

$$\vec{c}_{\mathrm{eq}}(\vec{x}) = F_t - F_z = 0, \quad F_t = 500i, \quad i = 2 \ldots 20. \tag{15}$$

The nonlinear inequality constraint $\vec{c}(\vec{x})$ is given by

$$\vec{c}(\vec{x}) = \begin{bmatrix} n\tau_m + (n-1)(\tau_p - \tau_m) - 250\,\mathrm{mm} \\ (2h_m + h_g) - 250\,\mathrm{mm} \\ 1.1\tau_m - h_m \end{bmatrix} \leq 0. \tag{16}$$

The first term limits the width of the permanent magnets to 250 mm and the second term constraints the total height. The third nonlinear inequality constraint limits the ratio between τ_m and h_m. The results of this optimization are shown in Figs. 10(a)–(c) and are discussed in Section 4.3.

4.2. Arrays with Unequal Dimensions

Figure 9 shows a 3D impression and cross-sectional view of a topology in which only one of the two magnet arrays is full-pitch, based on the basic topology in Fig. 5(d) [16]. The number of poles along the horizontal directions, n, is varied between 3 and 11. The bottom magnet array is full-pitch ($\tau_{m_1} = \tau_{p_1}$) and the upper array is fractional pitch ($\tau_{m_2} < \tau_{p_2}$). Further, both pole pitches, τ_{p_1} and τ_{p_2}, are not necessarily equal and the magnet height h_{m_2} may vary with respect to that of the bottom array, h_{m_1}. With inclusion of these new parameters the optimization is performed as described in Section 4.1. The maximum width and height of 250 mm are maintained. The results of this optimization are shown in Fig. 10(d) and are discussed below.

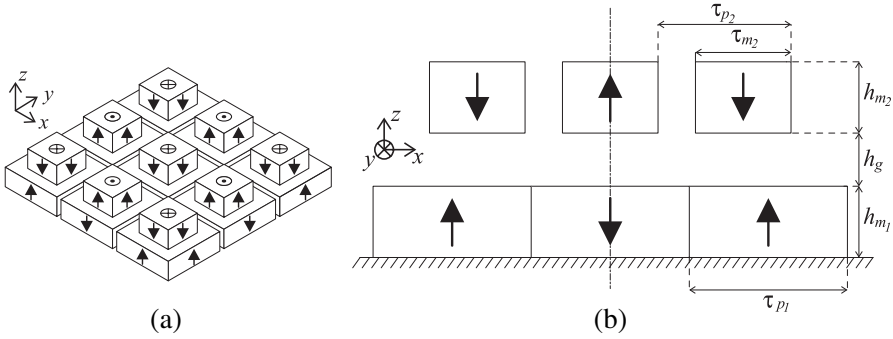

Figure 9. Schematic (a) 3D view and (b) cross-section with dimensions of the gravity compensator with unequal planar checkerboard arrays.

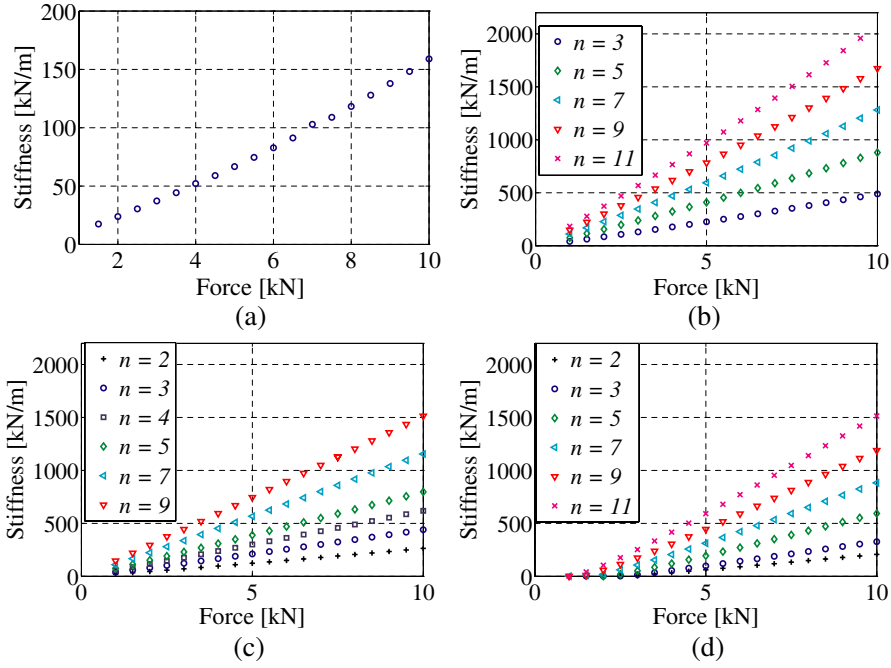

Figure 10. Force versus vertical stiffness K_{zz} of (a) the $n = 1$ topology, (b) the planar checkerboard array, (c) the planar quasi-Halbach topology and (d) the topology with unequal arrays.

4.3. Results and Discussion

Figure 10 shows the force versus stiffness characteristics for the aforementioned horizontal topologies. As a result of the nonlinear force constraint (15) the results are evenly spaced on the horizontal axis. Fig. 10(a) shows the minimization of the stiffness for $n = 1$, i.e., the topology of Fig. 7(a), which exhibits an almost linear relationship between the force level and the minimal stiffness. Similar properties are seen in Fig. 10(b) (the checkerboard pattern of Figs. 7(b)) and 10(c) (the quasi-Halbach pattern of Fig. 7(c)). It is observed that, unlike in devices which aim at maximizing force only, it seems not to be advantageous to employ a quasi-Halbach topology instead of a checkerboard topology, since the achievable minimum stiffness values are comparable.

The curves in Figs. 10(a)–(c) are almost first-order and seem to cross the origin. According (11), which describes the resonance frequency in terms of force and stiffness, this suggests that the resonance frequency depends on the number of magnets n and not on the required force level, as K_{zz}/F_z remains reasonably constant. It is observed that a high number of magnets in the given volume leads to an increased stiffness level, which corresponds to an elevated resonance frequency. As such, the high force densities that are obtained in this way are conflicting with the low-stiffness requirements and as such this topology is considered unsuitable for anti-vibration devices.

Figure 10 shows the force versus stiffness characteristic for the topology of Fig. 9. In comparison to Figs. 10(b)–(c) the stiffness has reduced, especially for topologies with high numbers of magnets. Especially at limited force levels up to approximately 2 kN the minimum stiffness of this particular topology is well below the values seen for the other topologies. According (11) the resonance frequency for force levels above 5 kN is in the order of 5–10 Hz, which is above the requirements for many advanced vibration isolation devices [1–4, 13–15]. As such, this topology seems especially suitable for applications which combine minimized stiffness with a limited force.

5. ARRAYS WITH VERTICAL AIRGAPS

A 90° rotation of Fig. 7(b) and a displacement according Fig. 6(a) results in a topology with a vertical airgap, shown in Fig. 11(a). There is only a vertical force component, parallel to the airgap, and therefore this checkerboard array becomes $1 \times n$, hence has only one pole in the horizontal direction. As discussed in Section 3.2 this configuration inherently exhibits zero vertical stiffness and therefore it is unnecessary to perform an optimization as described above, as long as the required

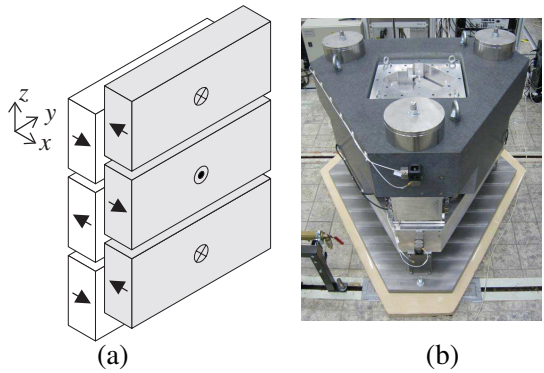

Figure 11. (a) 3D impression of the gravity compensator topology with vertical airgap and (b) impression of the realized test rig with a single gravity compensator supporting a 730 kg load.

vertical force is achieved. A force maximization within the given volume constraint has shown that the maximum studied force of 10 kN is indeed achievable within the given volume.

A prototype of an electromagnetic gravity compensator with fully passive, magnet-based gravity compensation has been realized and is shown in Fig. 11(b) [3]. This gravity compensator is based on the aforementioned topology with vertical airgaps and combines near-zero stiffness with a passive vertical force that supports a mass of 730 kg in a design that contains a total magnet volume of 1.7 dm^3. This unstable (permanent-magnet based) device is actively stabilized by actuators which consume less than 1 W. Its low stiffness has been experimentally measured and is approximately 1 kN/m, which corresponds to a passive vertical resonance frequency of 0.2 Hz. As such, it is confirmed that this topology is suitable to combine the conflicting requirements of high force and low stiffness successfully.

6. CONCLUSIONS

The analytical surface charge modeling technique represents a magnet by means of magnetically charged surfaces. A subsequent analytical calculation of the Lorentz force between these surfaces contains an abstraction that is helpful in the design of a permanent-magnet based gravity compensator for vibration isolation. The force between two magnets is related to their respective flux density on each other's surface, which is obtained by simply placing them at a short intermediate distance. A simultaneous reduction of the stiffness, however, is less intuitive and more difficult to achieve; it can only

be obtained if the gradient of one permanent magnet's field is small around the edges of the other permanent magnet. As such, the edges of the permanent magnets should be separated to reduce the stiffness.

By means of topology research these conclusions have been verified for multi-magnet gravity compensator topologies with a single airgap. It is found that topologies with equally sized and aligned permanent magnets show no potential to reduce the resonance frequency. A better compromise is found in topologies with unequally sized magnet arrays, which offer a stiffness reduction up to limited force levels. However, a virtual decoupling of force and stiffness is obtained by choosing a vertical airgap topology with displaced magnets. This topology is capable of combining a high force level with zero stiffness, which is very suitable for vibration reduction applications. Such topology has been realized in an experimental test setup, in which a mass of 730 kg is magnetically levitated with near-zero stiffness.

REFERENCES

1. Ibrahim, R. A., "Recent advances in nonlinear passive vibration isolation," *Journal of Sound and Vibration*, Vol. 314, 371–452, 2008.
2. Robertson, W. S., M. R. F. Kidner, B. S. Cazzolato, and A. C. Zander, "Theoretical design parameters for a quasi-zero stiffness magnetic spring for vibration isolation," *Journal of Sound and Vibration*, Vol. 326, 88–103, May 2009.
3. Janssen, J. L. G., "Extended analytical charge modeling for permanent-magnet based devices: Practical application to the interactions in a vibration isolation system," Ph.D. thesis, Eindhoven University of Technology, Eindhoven, The Netherlands, 2011.
4. Nagaya, K. and M. Sugiura, "A method for obtaining a linear spring for a permanent magnet levitation system using electromagnetic control," *IEEE Trans. on Magn.*, Vol. 31, 2332 –2338, May 1995.
5. Akoun, G. and J.-P. Yonnet, "3D analytical calculation of the forces exerted between two cuboidal magnets," *IEEE Trans. on Magn.*, Vol. 20, 1962–1964, Sept. 1984.
6. Bancel, F., "Magnetic nodes," *J. of Appl. Phys.*, Vol. 32, 2155–2161, Jun. 1999.
7. Janssen, J. L. G., J. J. H. Paulides, E. A. Lomonova, F. Bölöni, A. Tounzi, and F. Piriou, "Analytical calculation of interaction

force between orthogonally magnetized permanent magnets," *Sensor Letters*, Vol. 7, 442–445, Aug. 2009.

8. Allag, H. and J.-P. Yonnet, "3D analytical calculation of interactions between perpendicularly magnetized magnets: Application to any magnetization direction," *Sensor Letters*, Vol. 7, 486–491, Aug. 2009.
9. Furlani, E. P., *Permanent Magnet and Electromechanical Devices: Materials, Analysis And Applications*, 6th edition, Academic Press, London, 2001.
10. Ravaud, R. and G. Lemarquand, "Magnetic field produced by a parallelepipedic magnet of various and uniform polarization," *Progress In Electromagnetic Research*, Vol. 98, 207–219, 2009.
11. Yonnet, J.-P. and H. Allag, "Three-dimensional analytical calculation of permanent magnet interactions by 'magnetic node' representation," *IEEE Trans. on Magn.*, No. 99, 1, 2011.
12. Janssen, J. L. G., J. J. H. Paulides, and E. A. Lomonova, "Analytical force and stiffness calculations for magnetic bearings and vibration isolation," *Computer Field Models of Electromagnetic Devices*, 1st edition, 502–511, IOS Press, Amsterdam, 2010.
13. Puppin, E. and V. Fratello, "Vibration isolation with magnet springs," *Review of Scientific Instruments*, Vol. 73, 4034–4036, Nov. 2002.
14. Choi, K. B., Y. G. Cho, T. Shinshi, and A. Shimokohbe, "Stabilization of one degree-of-freedom control type levitation table with permanent magnet repulsive forces," *Mechatronics*, Vol. 13, 587–603, 2003.
15. Choi, Y.-M., M. G. Lee, D.-G. Gweon, and J. Jeong, "A new magnetic bearing using halbach magnet arrays for a magnetic levitation stage," *Review of Scientific Instruments*, Vol. 80, No. 045106, 1–9, 2009.
16. Janssen, J. L. G., J. J. H. Paulides, E. A. Lomonova, B. Delinchant, and J.-P. Yonnet, "Design study on magnetic springs with low resonance frequency," *Proc. of the LDIA 2011 Symp.*, Vol. 19, 1–6, Eindhoven, the Netherlands, 2011.